THE ASTROPHYSICAL JOURNAL, 250:200–212, 1981 November 1

THE ENERGETICS OF MOLECULAR CLOUDS. IV. THE S88 MOLECULAR CLOUD

NEAL J. EVANS II,[1,2,3] GUY N. BLAIR,[1,2,4,5] P. HARVEY,[6] FRANK ISRAEL,[7,8]
W. L. PETERS III,[1,2] M. SCHOLTES,[1] T. DE GRAAUW,[8] AND PAUL VANDEN BOUT[1,2]
Received 1981 March 19; accepted 1981 May 7

ABSTRACT

The S88 molecular cloud has been observed in several molecular lines and at infrared wavelengths from 1 to 100 μm. The CO emission has a single, sharp peak which is near the Hα emission region S88 B and centered on a compact H II region observed in the radio continuum. The infrared observations indicate that the principal luminosity source is located near the radio continuum peak and is hidden behind substantial extinction, presumably from the molecular cloud. The molecular cloud has a size of about 6.5 pc and a mass of $\sim 5 \times 10^3\ M_\odot$ at an assumed distance of 2 kpc. Regions of very high density ($\gtrsim 10^5$ cm^{-3}) do not seem to be present. Analysis of the energetics leads to a predicted dust cooling rate in good agreement with the infrared observations, which indicate $L = 1.8 \times 10^5\ L_\odot$. A more detailed examination of the energetics indicates that densities may be insufficient for collisions of molecules with warm dust grains to heat the gas to the observed kinetic temperature.

Subject headings: infrared: sources — interstellar: molecules — nebulae: H II regions

I. INTRODUCTION

This paper is the fourth in a series devoted to a study of the properties and energetics of molecular clouds. The overall objectives and methods of analysis were presented in Paper I (Evans, Blair, and Beckwith 1977); refinements of the techniques have been discussed in Papers II and III (Blair *et al.* 1978; Evans and Blair 1981). The methods used in this paper are essentially those of Paper III.

The S88 region has been studied previously by a number of investigators. Figure 1 shows the red print of the Palomar Sky Survey (PSS). The S88 nebula (Sharpless 1959) is itself a diffuse H II region with a very low emission measure (Wendker 1971), visible near the northwest edge of Figure 1. Two bright knots of nebulosity, S88 A and S88 B, lie to the southeast of S88 (Lortet-Zuckerman 1974), near the center of Figure 1. Radio continuum observations of S88 A and S88 B have been summarized by Felli and Harten (1981). No radio continuum emission from S88 A is seen to a level of 150 mJy at 5 GHz. Strong radio emission is observed from a compact H II region centered slightly to the east of the optically visible nebulosity S88 B. Felli and Harten (1981) interpret their 5 GHz continuum map in terms of two components, S88 B-1 and S88 B-2. Most of the flux at 5 GHz is due to S88 B-1, although the more easterly S88 B-2 has a very high electron density ($\geq 1.9 \times 10^4$ cm^{-3}) and emission measure ($\geq 1.8 \times 10^7$ pc cm^{-6}). The region that we have studied is centered on the optical nebulosity S88 B.

The S88 region was also detected as CRL 2455 in the wide beam ($3' \times 10'$) survey of Price and Walker (1976). More detailed infrared studies have been made by Zeilik (1977) and Pipher *et al.* (1977). Molecular line observations have been made for OH (Turner 1970), CO (Schwartz, Wilson, and Epstein 1973; Blair, Peters, and Vanden Bout 1975), and H_2O (Blair, Davis, and Dickinson 1978). The velocities of the CO emission (21–23 km s^{-1}) and OH absorption (21.8 km s^{-1}) agree with the 23.5 km s^{-1} velocity of Hα (Deharveng and Maucherat 1978) and with the 20.3 km s^{-1} velocity of the carbon recombination line, C167α (Silverglate and Terzian 1978) obtained in the direction of S88 B, indicating that the molecular cloud is physically associated with the H II region. There are small, but significant, shifts in the velocities of radio recombination lines relative to the molecular cloud velocity. The mean velocity of radio hydrogen recombination lines is 26.8 ± 0.2 km s^{-1} (Viner, Clark, and Hughes 1976; Silverglate and Terzian 1978). In addition, the diffuse Hα emission south of S88 B (see Fig. 1) has a mean velocity of 19.2 km s^{-1} (Deharveng and Maucherat 1978). Thus there is considerable evidence for flows of ionized gas at modest (~ 3 km s^{-1}) velocities relative to the molecular cloud. In addition, the H_2O maser had velocity features at 13.6, 14.8, and 30.0 km s^{-1}.

The stellar distance to S88 is 2.5 kpc (Georgelin 1975). The exciting star of S88 A has been identified as a B0.5 V star at a distance of 2.0 kpc (Crampton, Georgelin, and Georgelin 1978). The exciting star of S88 B has not been

[1] Department of Astronomy and Electrical Engineering Research Laboratory, The University of Texas at Austin.
[2] Visiting Astronomer, Kitt Peak National Observatory, which is operated by Association of Universities for Research in Astronomy, Inc., under contract with the National Science Foundation.
[3] Guest Investigator, Mount Wilson Observatory.
[4] ElectroMagnetic Applications, Inc.
[5] Netherlands Foundation for Radio Astronomy.
[6] Steward Observatory, University of Arizona.
[7] Owens Valley Radio Observatory, California Institute of Technology.
[8] Space Science Division, ESTEC, European Space Agency.

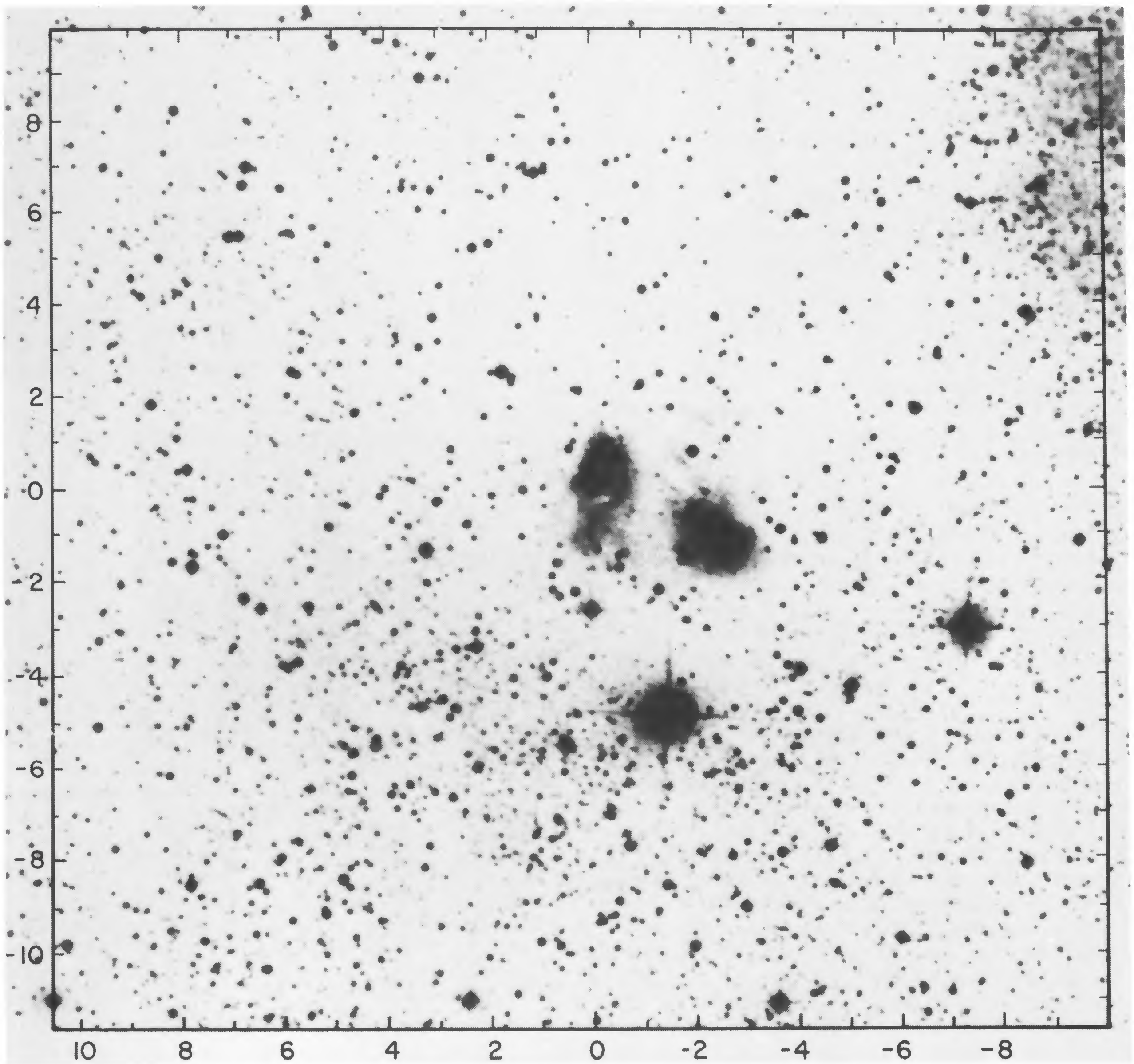

FIG. 1.—The red (PSS) print is reproduced at the approximate scale of the CO maps. The reference position is $\alpha = 19^h44^m40^s$, $\delta = +25°05'30''$ (1950). The offsets are in arc min. North is up and east is to the left. S88 is the diffuse region in the northwest corner. S88 B lies close to the reference position, while S88 A is displaced to the southwest.

identified. Because the molecular emission does not clearly extend to S88, but does seem to be intimately related to S88 A and S88 B, we adopt a distance of 2.0 kpc for the molecular cloud and for S88 B. S88 B lies at galactic coordinates of $l = 61\overset{\circ}{.}5$, $b = 0\overset{\circ}{.}1$.

II. OBSERVATIONS

a) *Molecular Line Observations*

Most of the $^{12}C^{16}O$(CO) and $^{13}C^{16}O$(^{13}CO) $J = 1$–0 data were obtained with the 4.9 m antenna of the Millimeter Wave Observatory[9] (MWO). Data on the $J = 2 \rightarrow 1$ transition of CO were also obtained at the MWO. The 11 m antenna of the National Radio Astronomy Observatory[10] at Kitt Peak (KP) was used to

[9] The Millimeter Wave Observatory is operated by the Electrical Engineering Research Laboratory, The University of Texas at Austin, with support from the National Science Foundation and McDonald Observatory.

[10] The National Radio Astronomy Observatory is operated by Associated Universities, Inc., under contract with the National Science Foundation.

obtain higher spatial resolution in the CO and ^{13}CO $J = 1 \rightarrow 0$ lines in selected regions, and to observe the $C^{18}O$ $J = 1 \rightarrow 0$ line. The $H_2{}^{12}C^{16}O$ $J_{K_{-1}K_1} = 2_{12} \rightarrow 1_{11}$ (2 mm H_2CO) line was observed at MWO. Observations of the $2_{11} \leftarrow 2_{12}$ (2 cm) and $1_{10} \leftarrow 1_{11}$ (6 cm) transitions of H_2CO were obtained with the 43 m telescope at the National Radio Astronomy Observatory (NRAO). The $1_{10} \leftarrow 1_{11}$ transition of H_2CO was observed with the Max Planck Institute (MPIfR) 100 m telescope at Effelsburg (Wilson, Snell, and Vanden Bout 1981). The observing parameters for these telescopes were summarized in Table 1 of Paper III.

We also observed the CO $J = 2 \rightarrow 1$ line using the Owens Valley Radio Observatory (OVRO) 10 m telescope (Leighton 1978) and the Estec heterodyne receiver (Lidholm and de Graauw 1979) at the Cassegrain focus. During the observations of S88, the receiver system temperature was 3500 K (SSB), and we used an integration time of 200 s per position, with a reference position 30′ away in azimuth. The transmission of the sky at the zenith was of order 85%, and an extended source beam efficiency (including all losses) of $50 \pm 5\%$ was found. Calibration of the system was effected using hot and cold load techniques; the sky emission was monitored frequently. We estimate the absolute calibration to be better than 20%. At the operating frequency of 230 GHz, the beamwidth (HPBW) was 26″ while rms pointing errors (measured on Jupiter, and also optically on selected stars) were of order 6″, but never more than 10″. Observations were obtained simultaneously in two filter banks, each having 256 channels, with channel resolutions of 1 MHz and 250 kHz, respectively (corresponding to velocity resolutions of 1.3 and 0.33 km s^{-1}).

Calibration of all the millimeter wavelength lines besides those observed at OVRO was achieved with a chopper wheel technique, and second order corrections were applied (Davis and Vanden Bout 1973). The resulting corrected antenna temperatures are denoted by $T_A{}^*$; they have been corrected for atmospheric attenuation and for antenna loss (ohmic, blockage, etc.). $T_A{}^*$, as used here, is not corrected for the coupling between the source and the main beam or for the forward spillover and scattering (cf. Kutner and Ulich 1981 for a definition of these quantities). The forward spillover and scattering efficiency (η_{FSS}) of the MWO antenna is 0.85 at $\lambda \sim 2$–3 mm and was 0.68 at 1.2 mm at the time of the observations. The situation on the KP antenna is more complex, because the substantial amount of power in an error beam implies that the coupling efficiency may depend on the source distribution in a complicated way. A value of 0.72 is appropriate for a source similar in distribution to OMC-1 (Ulich and Haas 1976). The MWO $J = 1 \rightarrow 0$ CO data and the MWO $J = 2 \rightarrow 1$ CO data are internally consistent when the above efficiencies are used. The KP $J = 1 \rightarrow 0$ CO data are systematically lower by about 30%, even after the lower efficiency is accounted for, and have not been used in the maps. The ^{13}CO $J = 1 \rightarrow 0$ data from KP are consistent with MWO data. The OVRO data are consistent in a broad sense, but the smaller beam reveals higher temperatures in parts of the source. Considering the various uncertainties, the absolute calibration of CO and ^{13}CO temperatures should be considered good to $\sim \pm 15\%$ (1 σ).

Calibrations of observations at centimeter wavelengths are free of some of the complications associated with the poor atmospheric transparency at millimeter wavelengths. In particular, the 6 cm observations of H_2CO can be considered to be reliably calibrated. The antenna temperature has been divided by the beam efficiency, η. The value of η for the NRAO 43 m telescope was taken to be 0.80 at 6 cm. At 2 cm wavelength, the 43 m telescope displayed serious degradation of efficiency. The efficiency was found to vary with elevation angle, as well as the source size. Furthermore, studies of objects which transit near 90° elevation angle showed that the efficiency was higher when the source was east of its transit than when it was west. The 2 cm H_2CO antenna temperatures have been divided by an efficiency factor determined from the mean elevation at which the source was observed and reference to the efficiency data presented by Snell (1981). Absolute calibration of T_A/η for the 2 cm H_2CO lines can be considered accurate only to $\pm 25\%$.

b) Infrared Observations

i) *Kitt Peak Observations*

The region enclosed by the small dashed lines in Figure 2 was surveyed at 2.2 μm with the 1.3 m telescope of the Kitt Peak National Observatory. The technique described in Paper I was used for finding sources. Nine sources were found with flux densities greater than 0.2 Jy at 2.2 μm. Little further information was obtained on any of these sources except for the source near the CO peak. Some of the other sources appear to be visible stars; however, the positions are poorly determined ($\pm 50''$), as

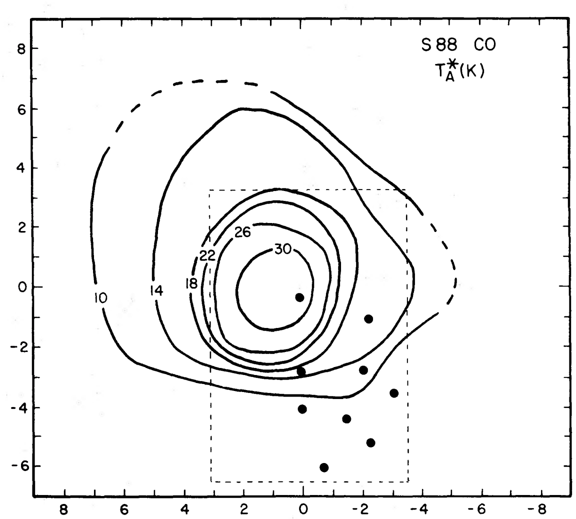

FIG. 2.—Contour diagram of $T_A{}^*$ for the CO emission. The reference position and offsets are as in Fig. 1. The dashed lines indicate regions where the map is incomplete. The box enclosed by the small dashed lines indicates the region searched at 2.2 μm, and the solid circles represent the sources which were found.

they are based only on their location in the original search grid.

The source near the CO peak was found to be extended and was mapped in more detail at 1.6, 2.2, and 3.5 μm. The maps were obtained with a beam size of 16″ and a chopper throw of 150″ north-south. For part of the map, this chopper throw introduced a star into the reference beam. This section of the map was redone with a 100″ chopper throw. The maps were obtained under computer control by position switching on a grid with positions separated by 10″; each map is based on 192 positions. The relative pointing was checked by periodically returning to the center position under computer control and checking the location of an offset guide star. The relative pointing appeared to be good to 3″–5″. The absolute position of the map was determined by offsetting from a nearby SAO star. The stars marked 1 and 3 on the 1.6 and 2.2 μm maps can be identified with stars 1 and 3 in the paper by Pipher *et al.* (1977). The positions of these stars in our map agree with the positions given by Pipher *et al.* to within about 5″. Star 2 of Pipher *et al.* is not apparent in our maps or in those of Pipher *et al.* The peak of the 3.4 μm map appears to be shifted northward by ~ 5″–10″ relative to the 2.2 μm and 1.6 μm peaks. The peak of the 12.6 μm map of Pipher *et al.* also appears to be shifted northward by about 10″–15″, so the effect seems real. The maps were calibrated by observations of standard stars and the peak flux densities at 2.2 and 3.4 μm are in reasonable agreement with the photometric observations of Pipher *et al.* (1977). Photometry was obtained at the positions of several of the peaks in the maps. A 16″ beam size was used with a 150″ chopper throw.

Spectrophotometry of the Bγ and Bα lines was obtained using the 2.1 m telescope of the Kitt Peak National Observatory. The telescope was pointed toward the 2 μm peak. The beam size was 11″, and the chopper throw was 30″. At the wavelength of Bγ, the resolution of the filter wheel was 0.028 μm and the data were taken at intervals of 0.0145 μm. At the wavelength of Bα, the resolution was 0.085 μm and the data were taken at intervals of 0.028 μm. Calibration was achieved by comparison to the standard stars, ζ Oph and α Vir.

ii) *Mount Wilson Observations*

Near-infrared and middle-infrared observations were obtained with the 1.5 m telescope of the Mount Wilson Observatory. The techniques and equipment for photometry have been described by Beckwith *et al.* (1976). Observations were obtained with a beam size of 9″ and a chopper throw of 25″ along a north-south line. Beam sizes of 14″ and 16″ were used for a few measurements.

iii) *Kuiper Airborne Observatory Observations*

Far-infrared observations were obtained from the Kuiper Airborne Observatory in 1979 August. The University of Arizona two channel photometer was used with a 37″ beam. The instrumental parameters have been described by Evans *et al.* (1981) and in more detail by Harvey (1979). The chopper spacing for these observations was 9′ along a SE–NW line. (The angle between the line of chopping and east was 54° to the south.) The average water vapor column was 18 precipitable μm along the line of sight to the source. Calibration was accomplished by observations of Mars, corrected for the differing water vapor columns. Extinction coefficients of 0.03 and 0.04 nepers per precipitable μm of water vapor were assumed at 50 and 100 μm, respectively (S. Whitcomb, private communication). Brightness temperatures for Mars were taken from Wright (1976). Calibration uncertainties were assumed to be 20% for the flux densities and 10% for relative flux densities used to obtain dust temperatures. Positions were determined by offset guiding on an SAO star visible in the focal plane. The absolute position of the maps should be good to ±10″.

III. RESULTS

a) CO *and* ^{13}CO

The CO results are shown in Figure 2, as a contour map of T_A*. The contours are based entirely on data taken at the MWO. Only a single velocity component at 21–23 km s^{-1} is seen in this region, and the profiles generally appear to be centrally peaked with no strong evidence for self-absorption (see Fig. 3). A low velocity wing, present at a few positions, will be discussed later. The central velocities show no strong evidence for a velocity gradient. Measurements with a 1′.2 beam of the $J = 2 \rightarrow 1$ CO line at the peak position gives the same result as the $J = 1 \rightarrow 0$ line for the excitation temperature to within the uncertainties. The assumption that the $J = 1 \rightarrow 0$ lines are optically thick and thermalized, at least near the peak, is well supported. The appearance of the CO map is remarkable among such maps for its simplicity. The single

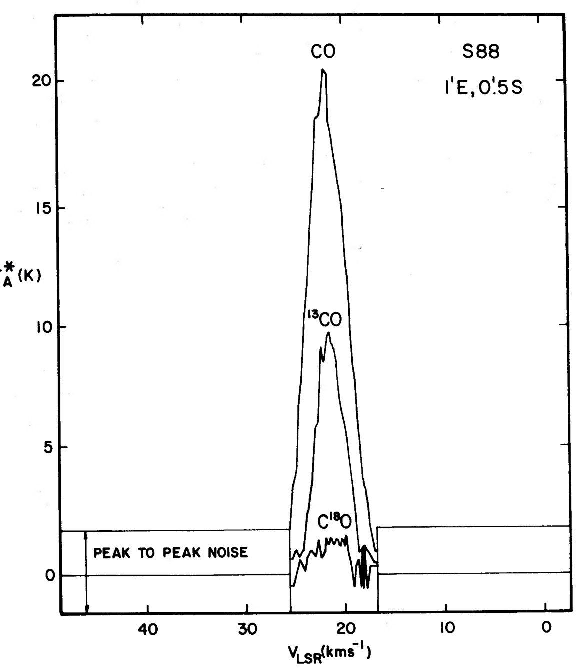

FIG. 3.—Spectra of the $J = 1 \rightarrow 0$ CO, ^{13}CO, and C^{18}O lines obtained at Kitt Peak. The CO line is about 30% lower than expected from MWO data. The position (1′ E, 0′.5 S) is the position of strongest ^{13}CO emission.

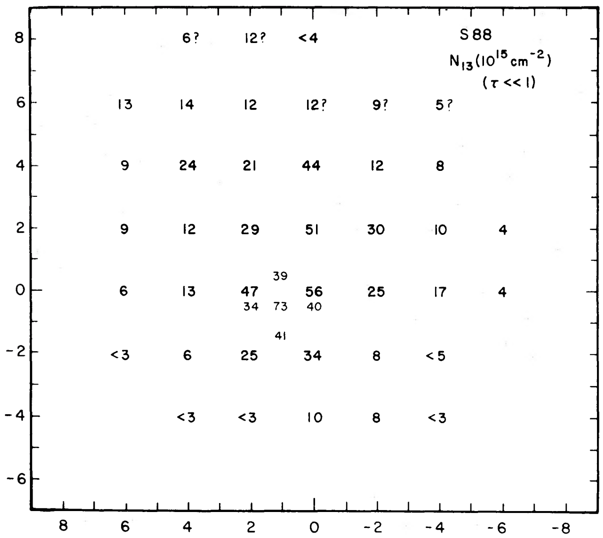

FIG. 4.—Column densities of ^{13}CO in units of 10^{15} cm^{-2}. The reference position and offsets are as in Fig. 1. The numbers in slightly smaller print size are based on Kitt Peak data.

strong peak is observed near the S88 B H II region; the emission falls off very rapidly to a level of $T_A^* \sim 10$–14 K, at which point a more extended plateau is seen. Even this plateau is quite compact (extent $\lesssim 10'$), but the map is incomplete in some directions, so more extensive emission cannot be ruled out. The peak emission is seen toward the radio H II region associated with S88 B. The 14 K contour includes the position of S88 A ($\sim 2'$ W, 1′ S), and a slight bulge in the contour suggests that S88 A may contribute very weakly to the heating. The OVRO data provide information on a smaller spatial scale and will be considered later in the paper.

The ^{13}CO results are presented in Figure 4, in the form of a grid of numbers representing the column density of ^{13}CO (N_{13}) in units of 10^{15} cm^{-2}. Data from MWO and KP are represented. The column densities were derived from the relation in Paper I, with T_A^* replaced by T_A^*/η_{FSS}; the fraction of the ^{13}CO population in the $J = 1$ state (f_1) was taken equal to 0.26 (Paper I). The relation used to get N_{13} relies on the assumption that the ^{13}CO optical depth (τ_{13}) is small. This assumption was checked by using the LTE approximation; τ_{13} was less than 0.5 at almost all positions, implying that corrections of less than 30% would be necessary. N_{13} was also determined using the LTE approximation; the ratio of N_{13}(LTE) to $N_{13}(\tau \ll 1)$ ranged from 0.7 to 1.8. The cases with large ratios were not positions with large τ_{13} but instead were positions of high T_K. When T_K is large, the LTE approximation is likely to overestimate N_{13} because it uses an infinite density expression for the partition function. Model calculations show that this expression overestimates N_{13} unless the density is very high.

The general features of the N_{13} map correspond to those of the T_A^*(CO) map. The region of high $N_{13}(\gtrsim 30 \times 10^{15}$ cm^{-2}) is concentrated into a small area near the CO peak and a plateau of $N_{13} = 10$–20×10^{15} cm^{-2} extends over a similar area to that covered by the plateau of CO emission. Thus the H II region lies near a peak of column density as well as a kinetic temperature peak.

b) H_2CO

The observations of the 6 cm H_2CO transition ($J_{K_{-1}K_1} = 1_{10} \leftarrow 1_{11}$) are presented in Table 1. The data from the 43 m NRAO telescope cover the region of the CO map except for the lack of a position $\sim 6'$ E of the reference position. The strongest absorption line occurs near the position of the CO peak and the H II region, but absorption is also seen north and probably west of the peak, where no radio continuum radiation is present. Conditions in these portions of the cloud are thus suitable for the pumping mechanism which cools this transition, suggesting densities of roughly 10^3 cm^{-3}. The higher absorption at the center position may be due to the presence of the H II region as a background source. With a flux density of $\sim$ 6 Jy, the H II region would produce an antenna temperature of $\sim$ 1.6 K on the NRAO antenna. In this situation it is hard to separate the absorption of the H II region from that of the cosmic background radiation.

Observations of the 2 mm ($J_{K_{-1}K_1} = 2_{12} \rightarrow 1_{11}$) and 2

TABLE 1

6 CENTIMETER FORMALDEHYDE RESULTS

	43 m TELESCOPE			100 m TELESCOPE		
OFFSET (arcmin) (1)	T_A/η[a] (K) (2)	V_{LSR} (km s^{-1}) (3)	ΔV (km s^{-1}) (4)	T_A/η[b] (K) (5)	V_{LSR} (km s^{-1}) (6)	ΔV (km s^{-1}) (7)
1′ E, 6′.5 S	<0.10	...	...	...	...	...
1′ E, 2′.5 S	...	...	...	−0.14(0.04)	22.5	5.0
5′W, 0′.5 S	∼ −0.10	22.1	2.0	...	...	...
1′ E, 0′.5 S	−0.30	21.0	3.0	...	...	...
1′ E, 0′.5 N	...	...	...	−0.48(0.04)	21.5	3.6
1′ E, 5′.5 N	−0.20	21.3	2.0	...	...	...

[a] $\eta = 0.80$; 1 σ uncertainty is $\sim$0.04 K for detections; upper limits are 2 σ.

[b] Elevation-dependent corrections for η and atmospheric attenuation have been applied; 1 σ uncertainties are in parentheses.

TABLE 2

FORMALDEHYDE RESULTS[a]

	2 MILLIMETER			2 CENTIMETER		
OFFSET (arcmin) (1)	$T_A{}^*$ (K) (2)	V_{LSR} (km s^{-1}) (3)	ΔV (km s^{-1}) (4)	T_A/η[b] (K) (5)	V_{LSR} (km s^{-1}) (6)	ΔV (km s^{-1}) (7)
0′ E, 2′ S	<0.7	...	...	...	...	...
1′ E, 0.′5 S	≤0.4	22.7	2.9	−0.10(0.01)	21.6	3.2
0′ E, 0′ N	0.8(0.3)	22.5	3.2	...	...	...
1′ W, 0′ N..........	≤0.7	22.2	2.5	...	...	...
1′ E, 0.′5 N	<0.9	...	...	...	...	...
1′ E, 1.′5 N	...	...	...	−0.06(0.02)	21.5	1.5
1′ E, 2′ N	<0.8	...	...	...	...	...
0′ E, 2′ N	<0.8	...	...	...	...	...
1′ E, 3.′5 N	...	...	...	<0.07	...	...

[a] The numbers in parentheses are measures of the noise per channel (1 σ); upper limits are 2 σ.
[b] η was determined from calibration curves given by Snell (1981.

cm ($J_{K_{-1}K_1} = 2_{11} \leftarrow 2_{12}$) transitions are summarized in Table 2. The absence of strong 2 mm emission suggests that the densities in the vicinity of the CO peak are not very high ($n \gtrsim 10^5$ cm^{-3}). This is somewhat surprising in view of the very high electron density ($n_e \geq 1.9 \times 10^4$ cm^{-3}) derived for the H II region component S88 B-2 (Felli and Harten 1981). A density of $n_e \approx 10^4$ cm^{-3} was also derived for parts of the S88 B optical nebula from observations of the [S II] doublet (Deharveng and Maucherat 1978). This point is discussed in § IV. More sensitive searches for 2 mm emission would be worthwhile.

c) Near- and Middle-Infrared

The maps of the source located near the CO peak are presented in Figure 5. The 2.2 μm map is consistent with that of Pipher *et al.* (1977) but is considerably more extensive. It covers essentially the entire optical nebulosity as well as the region of radio emission. There is an extended component with a strong central peak (P in Fig. 5) and several discrete sources. Stars 1 and 3 in the map of Pipher *et al.* were detected in our 1.6 and 2.2 μm maps. Star 2 was apparent neither in our 2.2 μm map nor in that of Pipher *et al.* It may be showing up in the 1.6 μm map as a westward extension of the contours. The blue print of the PSS (Fig. 5*e*) shows a fourth star east of star 1, and this star may show up at 1.6 and 2.2 μm as an eastward extension in the contours. A fifth starlike object appears in our 2.2 μm map in a region not covered by Pipher *et al.* This source is also clearly seen at 1.6 μm and possibly at 3.4 μm. No star is shown at this position by Deharveng and Maucherat (1978), nor is anything visible in Figure 5*e*. The 3.4 μm map looks rather different in that the stars are not as obvious, and there is an extension southeastward from the peak and possibly a secondary maximum, marked by an S in the 3.4 μm map. The peak is also shifted slightly to the north, as noted in § II, and there is an overall shift to the east.

Photometry was obtained at the positions marked P, S, 1, and 5, and is presented in Table 3. The results at 2.2 and 3.4 μm for position P are in reasonable agreement with those of Pipher *et al.* (1977) and with the mapping results. The 10 μm results are about one-fifth the values given by Pipher *et al.*, who used a larger beam and chopper throw; thus the 10 μm emission seems to be mostly from an extended component. The spectrophotometry at position P yielded line fluxes $F(\mathrm{B}\alpha) = (2.1 \pm 0.2) \times 10^{-14}$ W m^{-2} and $F(\mathrm{B}\gamma) < 2 \times 10^{-14}$ W m^{-2}. These values are consistent with the results of Pipher *et al.* (1977), when correct values of their spectral resolution are used (Pipher, private communication). A new reduction of their data yields $F(\mathrm{B}\alpha) = (3.1 \pm 0.6) \times 10^{-14}$ W m^{-2}

TABLE 3

INFRARED PHOTOMETRY[a]

Position	J(1.2 μm) (Jy)	H(1.6 μm) (Jy)	K(2.2 μm) (Jy)	L(3.4 μm) (Jy)	10 μm BB (Jy)	Beam (arcsec)	Chopper Throw (arcsec)
P	...	0.034 ± 0.003	0.161 ± 0.009	0.82 ± 0.13	2.3 ± 0.4	9	25
	0.041 ± 0.004	0.070 ± 0.007	0.22 ± 0.02	1.0 ± 0.1	...	16	150
S	...	...	...	0.8 ± 0.2	...	16	25
	...	...	...	...	2.4 ± 1.0	14	25
1	0.116 ± 0.010	0.122 ± 0.009	0.113 ± 0.007	<0.6 (3 σ)	<3.0 (3 σ)	9	25
5	...	0.032 ± 0.004	0.103 ± 0.005	0.2 ± 0.1	<1.3 (3 σ)	9	25

[a] Photometry was obtained after peaking up at 2.2 μm on positions P, 1, and 5. An offset was used to move to position S. Uncertainties are ±1 σ, but are often due to calibration uncertainties, taken to be ±10%.

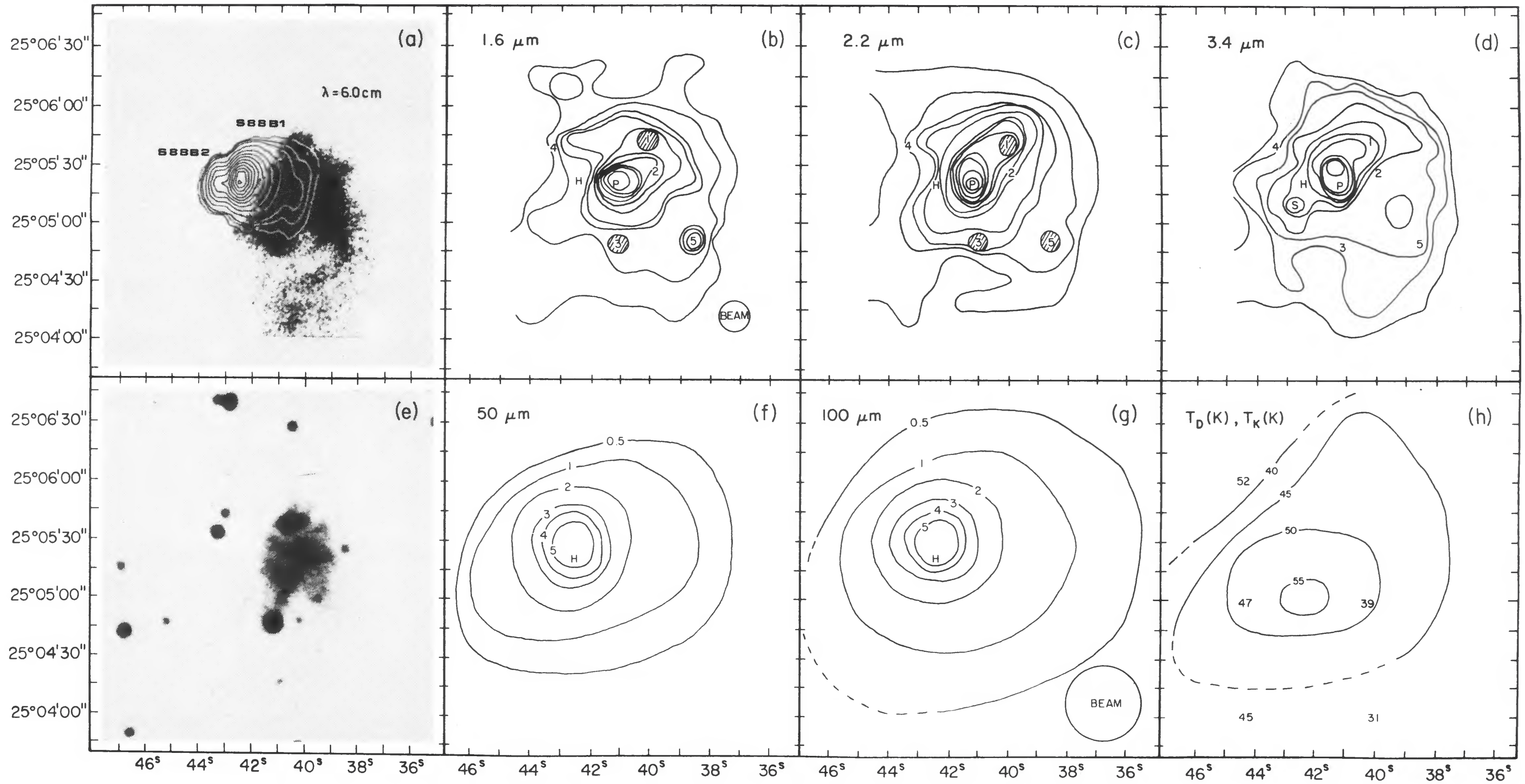

FIG. 5.—From top left to top right: (*a*) the 6 cm radio continuum contours superposed on an Hα photograph (both from Felli and Harten 1981); (*b*), (*c*), (*d*) infrared intensity contours at 1.6, 2.2, and 3.4 μm. From bottom left to bottom right: (*e*) the blue print of the Sky Survey; (*f*), (*g*) 50 and 100 μm intensity contours; (*h*) contours of T_D(K) and values for T_K(K). Note that the scale for right ascension is slightly different for the two photographic panels. Notes on each map follow. (*b*) The 1.6 μm map has a lowest contour level of 0.015 Jy per beam (= 3 σ) and a contour interval of 0.010 Jy per beam. The positions of four stars visible in Fig. 5*e* are indicated by the numbers 1–4. The letter H marks the peak of the H II region radio emission (Fig. 5*a*) and the P marks the 2.2 μm peak. The filled circles represent stars 1 and 3, and the contours around these stars are not shown. (*c*) The lowest contour on the 2.2 μm map is 0.020 Jy per beam (= 3 σ) and contours are spaced by 0.015 Jy per beam. The inner four contours around the peak are spaced by 0.030 Jy per beam. The two filled circles with numbers are as in Fig. 5*b*, and a third filled circle represents a strong point source (No. 5) which can also be seen on the 1.6 μm map. (*d*) The lowest contour on the 3.4 μm map is 0.12 Jy per beam (= 3 σ), and contours are spaced by 0.09 Jy per beam. The beams for Figs. 5*b*, 5*c*, and 5*d* are given in Fig. 5*b*. Those for Figs. 5*f* and 5*g* are given in Fig. 5*g*.

and $F(\mathrm{B}\gamma) = (4.0 \pm 0.7) \times 10^{-15}$ W m^{-2} (Pipher, private communication). The larger Bα flux observed by Pipher *et al.* is consistent with their larger beam (17″ compared to our 11″).

d) Far-Infrared

The maps of emission at 50 and 100 μm are also presented in Figure 5. Compared to the near-infrared maps, the far-infrared emission is smoother and more symmetric spatially, although this may be caused in part by the large beam size (37″ as opposed to 16″). However, the extent of the far-infrared emission is very similar to that of the near-infrared emission. Considering contours where the emission has fallen to 0.5 and 0.2 of the peak value, the area enclosed is very similar at 3.4, 50, and 100 μm. The far-infrared peaks are shifted eastward from the peaks in the near-infrared maps and lie closer to the peak of the H II region S88 B-1 (marked by an H in Fig. 5).

e) Energy Distribution and Extinction

The total flux densities were obtained by integrating the contour maps at 1.6, 2.2, 3.4, 50, and 100 μm. The results are plotted in Figure 6. Also plotted are the data from the AFGL catalog at 11, 19.8, and 27.4 μm (Price and Walker 1976) and the integrated 12.6 μm flux density from Pipher *et al.* (1977). The latter lies considerably below the AFGL flux density, a fact which Pipher *et al.* attribute to the presence of diffuse emission that they did not detect. Since they used a chopper throw of 60″ for the

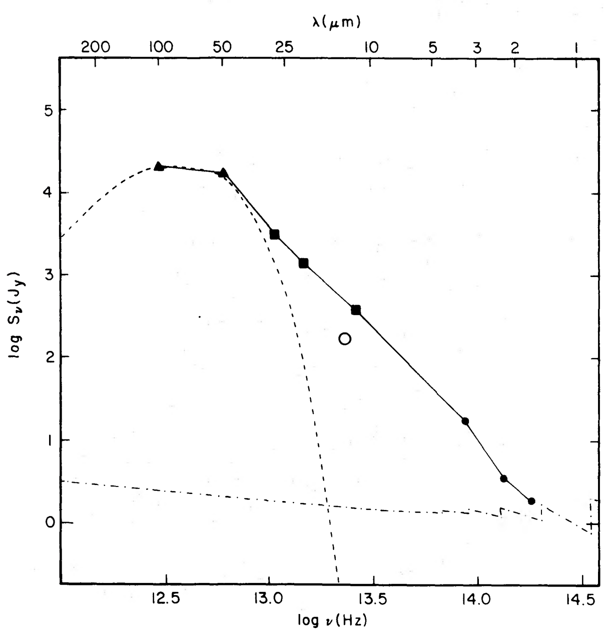

FIG. 6.—Spectral energy distribution of the emission from S88 B. The triangles represent the total flux densities at 50 and 100 μm, obtained by integrating the maps in Fig. 5. Likewise the filled circles represent the total fluxes at 1.6, 2.2, and 3.4 μm. The open circle is the integrated flux density given by Pipher *et al.* at 12.6 μm, and the squares are taken from the AFGL survey. The dashed line is the emission expected from dust at 48 K, radiating with a λ^{-1} emissivity law. The dash-dot line is the emission expected from the ionized gas.

12.6 μm map, this interpretation is quite plausible in view of the extent of the source at 3.4 and 50 μm. Consequently, we will use the AFGL data in integrating the energy distribution to obtain the luminosity.

The integrated far-infrared flux densities yield an average dust temperature $\langle T_D \rangle = 48 \pm 3$ K if a λ^{-1} emissivity law is assumed. The dashed line in Figure 6 is the expected emission from such dust, normalized to match the far-infrared emission. It is clear from the figure that a single temperature cannot explain the energy distribution. A substantial amount of dust at $T_D > 48$ K must exist to account for the near- and middle-infrared emission. Indeed, the approximately power law behavior of the spectrum shortward of 50 μm is characteristic of optically thin emission from dust heated to a range of temperatures (Scoville and Kwan 1976) and is a common feature of well-developed H II regions (cf. Beckwith *et al.* 1976).

The radio observations and the calculations of Ferland (1980) were used to predict the free-free and free-bound emission from the ionized gas. The predicted emission is less than the total observed emission at $\lambda \geq 1.6$ μm (see Fig. 6). This situation is suggestive of the presence of quite warm dust. The presence of this dust is also suggested by the fact that the near-infrared emission is considerably more extended than the radio continuum emission (see Fig. 5). The sharp cutoff in the optical emission indicates a rapid variation in the extinction with position. The fact that the near-infrared emission is displaced from the radio continuum peak (H in Fig. 5) toward the optical emission indicates that the extinction is appreciable at near-infrared wavelengths as well as in the visible. Comparison of the maps in Figure 5 shows that the centroid of the infrared emission shifts toward position H as the wavelength increases. All these facts are consistent with the view that the near-infrared maps have been significantly distorted by the presence of extinction in front of the H II region.

Quantitative estimates of the extinction are complicated by several factors. The extinction obviously varies rapidly between the position of the radio peak H and the position of the near-infrared peak P. Also, the evidence that the near-infrared emission is not due primarily to the ionized gas renders suspect any attempt to compare the near-infrared emission predicted from the radio to the observed near-infrared emission. The estimate of $A_v = 19$ mag by Pipher *et al.* (1977) suffers from both these problems, while their estimate of 17 mag based on a comparison of the Bγ line strength to that predicted from the free-free emission suffers from the first problem.

Another way to estimate the extinction is from the ^{13}CO observations. Dickman (1978) found a relation between A_v and N_{13}(LTE), the ^{13}CO column density derived assuming LTE. For consistency with Dickman, we used the LTE method to derive $N_{13}(\mathrm{LTE}) \approx 10^{17}$ cm^{-2} at the positions closest to that of the compact H II region, resulting in an estimate of 40 ± 20 mag. Extinctions about half this large would be implied from the average N_{13} for the inner few shells of the molecular cloud. Similar values are obtained from the 100 μm

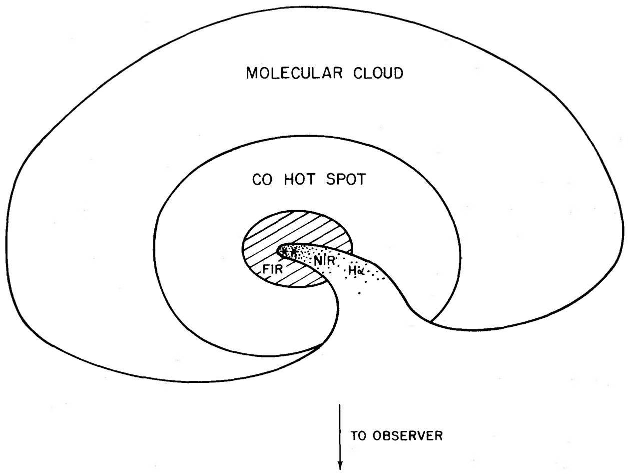

FIG. 7.—Schematic model for the source. The molecular cloud envelops the exciting stars of the compact H II regions S88 B-1 and S88 B-2. An opening in the cloud allows some of the ionized region to be seen as the Hα emission region S88 B. Near-infrared emission comes from the ionized gas and hot dust located in the H II region, while far-infrared emission comes from a larger region in the surrounding molecular cloud, and the CO peak surrounds the region seen in the far-infrared. S88 and S88 A are not represented.

optical depth, if the ratio of visual opacity to 100 μm opacity is $\sim$ 650–1600 (cf. Whitcomb, Hildebrand, and Keene 1980). Since the molecular cloud extends well beyond the Hα emission region, it must lie behind that region, but at least partly in front of the center of the radio emission. This morphology suggests that the Hα region represents a cavity in the front face of the molecular cloud. The exciting star could be located near the radio continuum peak and hidden from view at optical and near-infrared wavelengths by the molecular cloud. Figure 7 shows one possible geometry for this region which satisfies the above constraints.

Another possible measure of the extinction to the position of peak infrared emission (P) is available by comparing the ratio of Bα and Bγ fluxes to theoretical predictions for their ratio. This leads to an estimate of the reddening between 2.17 and 4.05 μm, $A_\gamma - A_\alpha = 1.1 \pm 0.4$ mag. From considering various estimates of the reddening law, we find $A_v = (18 \pm 5) \times (A_\gamma - A_\alpha)$. Thus, the estimated $A_v = 20 \pm 9$ mag. This value is consistent with the estimate based on ^{13}CO, especially since position P is in a less extinguished portion of the region than is position H.

IV. PHYSICAL PROPERTIES OF THE MOLECULAR CLOUD

The properties of the molecular cloud were determined according to the methods described in Paper III. Briefly, the contours of T_A*(CO) are used to define shells of the cloud, assuming spherical symmetry. The average T_K and N_{13} within the ith shell are determined from observations lying between the ith contour and the $(i-1)$th contour. The mass of ith shell was obtained from $M_i = \langle N_{13} \rangle_i \Delta a_i / X(^{13}\text{CO})$, where $\Delta a_i = a_i - a_{i-1}$ is the area on the sky between the ith and the $(i-1)$th contour, and $X(^{13}\text{CO}) = 2 \times 10^{-6}$ (Dickman 1978). The average density along the line of sight is obtained from $\langle n \rangle_i = \langle N_{13}' \rangle_i [X(^{13}\text{CO}) l_i]^{-1}$, where $\langle N_{13}' \rangle_i$ is the average over *all* N_{13} inside the ith contour and l_i is the path length through the center of the ith contour, again assuming spherical symmetry.

The results are presented in Table 4. The total size of the cloud [measured to the 10 K contour of T_A*(CO)] is 6.5 pc, very similar to the sizes of other clouds studied in this series of papers. The total mass is 5×10^3 $M_\odot$, again comparable to the other clouds. As can be seen in Table 4, the contributions from the outermost two shells are the largest and the total mass may be much larger if much more extensive CO emission exists. Extensive maps at low resolution would be of great interest.

The average density rises from 700 to $\sim 6 \times 10^3$ from the outermost to the innermost contour. The peak value may be consistent with the failure to detect strong emission in the 2 mm H_2CO line. This situation is in sharp contrast to that found in the other clouds in this study where 2 mm H_2CO emission was seen near the peak. In the other clouds, the H_2CO observations allowed us to infer densities of 10^5 cm^{-3} or greater, typically 100 times higher than the $\langle n \rangle$ inferred from ^{13}CO. The values of $\langle n \rangle$ in Table 4 are consistent with a density law going roughly as $r^{-1.4}$ whereas other sources

TABLE 4

PHYSICAL PROPERTIES OF THE S88 MOLECULAR CLOUD

Shell No. (1)	T_A*(CO) (K) (2)	a_i (pc^2) (3)	T_K (K) (4)	l_i (pc) (5)	$\langle N_{13} \rangle$ (10^{15} cm^{-2}) (6)	M ($M_\odot$) (7)	$\langle n \rangle$[b] (10^2 cm^{-3}) (8)
1	30	1.5	39	1.4	48 ± 14	540	57
2	26	4.9	34	2.5	33[a]	830	29
3	22	6.6	29	2.9	38 ± 12	480	25
4	18	9.0	25	3.4	28[a]	500	21
5	14	20	20	5.1	20 ± 12	1600	11
6	10	33	15	6.5	11 ± 3	1000	7
Total	...	...	...	...	...	5000	...

[a] Too few measurements of N_{13} exist between these contours to determine a dispersion.
[b] For determining $\langle n \rangle$, the average of *all* N_{13} within the contour was used.

suggest r^{-2}. Thus the S88 molecular cloud may lack the steep density gradient and high density core which characterize the other sources in this study. Alternatively, the fairly luminous star (see below) may have destroyed the H_2CO in the dense region of the cloud.

In contrast to the modest peak densities in the S88 molecular cloud, the peak T_K is quite high, 39 K for the innermost contour. This is the highest peak temperature measured in this study, and the small beam maps made at OVRO indicate that even higher temperatures exist.

V. ENERGETICS: GLOBAL CONSIDERATIONS

As discussed in Papers I, II, and III, the physical properties of the cloud deduced in § IV will be used to estimate the gas cooling rate of each shell. Based on the assumption that the gas is heated by collisions with the dust, the dust temperature T_D will be assumed equal to the gas kinetic temperature T_K. The far-infrared optical depth, τ(FIR), will be estimated from the ^{13}CO column density, and a dust cooling rate for the ith shell, C_i (dust), can be predicted from T_D, τ(FIR), and s_i, the surface area of the ith shell. The predicted total dust cooling rate will then be compared to the observed luminosity.

The gas cooling rate of each shell, shown in Table 5, is computed from $C_i(\text{gas}) = \Lambda_i(\text{gas})\Delta v_i$, where Λ_i(gas) is the cooling rate per unit volume and Δv_i is the volume in the ith shell. Cooling rates have been calculated by Goldsmith and Langer (1978); these rates depend on density and temperature. Using an interpolation of their rates, we calculated Λ_i(gas) for each shell using the values of T_K and $\langle n \rangle$ in Table 4. The total cooling rate is 6.2 $L_\odot$. Shells with $T_K < 20$ K may be heated primarily by global processes such as cosmic rays. For regions above 20 K, local heat sources are necessary. Goldreich and Kwan (1974) suggested that young stars and protostars heat the dust in the molecular cloud and the gas is heated by collisions with the dust. A minimum T_D equal to T_K is implied by this process.

The assumption that $T_D = T_K$ allows us to predict a minimum cooling rate for the dust. The dust cooling rate for the ith shell is computed from $C_i(\text{dust}) = \sigma_{SB} T_D{}^4 \tau_i(\text{FIR}) s_i$, where σ_{SB} is the Stefan-Boltzmann constant and s_i is $4a_i$ if the cloud is spherically symmetric. Two estimates of the far-infrared optical depth are given in Table 5. The first is calculated from $\tau_i(\text{FIR}) = 10^{-18}\langle N_{13}\rangle_i$ (Paper I). As noted in Paper III, this method may overestimate the optical depth since $\langle N_{13}\rangle_i$ applies to the whole line of sight through the cloud. A second estimate, $\tau_i'(\text{FIR}) = 10^{-18}\langle N_{13}'\rangle_i(l_i - l_{i-1})/l_{\max}$, is also given in Table 5, where $l_{\max}$ is the size of the largest contour considered and $\langle N_{13}'\rangle_i$ is the average over *all* N_{13} inside the ith contour. Two estimates of the cooling rate (C_i and C_i'), using the two different estimates of optical depth, are also given in Table 5. The total dust cooling rate is predicted to be 0.7–3.8 × 10^5 $L_\odot$, including all shells. In this case the outermost shell contributes less than 10% of the total. As discussed in Paper III, C_i' would provide a better estimate for the cooling if the cloud is homogeneous, while C_i would be more appropriate in the presence of a strong density peak.

The energy distribution in Figure 6 can be integrated to give a total flux of 1.4 × 10^{-9} W m^{-2} between 1.6 and 100 μm. Eighty-five percent of the total is due to emission between 27 μm and 100 μm which is likely to arise in the molecular cloud. The contribution from wavelengths longer than 100 μm can be estimated by assuming $T_D = 48$ K and a λ^{-1} emissivity law to be 2.5 × 10^{-10} W m^{-2}. Larger contributions may be present if significant amounts of cooler dust exist. Assuming spherically symmetric emission at the assumed distance to the source of 2 kpc, the inferred luminosity is 1.8 × 10^5 $L_\odot$. This result lies midway between the two predictions given above. This result is consistent with the suggestion of Goldreich and Kwan (1974) regarding the heating source for the gas.

The dust cooling rate is clearly very large and implies an equal heating rate to achieve steady state. The radio continuum flux of 6.1 Jy (Felli and Harten 1981) implies a Lyman continuum photon flux of 2.1 × 10^{48} s^{-1}, using relations given by Matsakis *et al.* (1976). This corresponds to a star with a luminosity of 6.6–8.3 × 10^4 $L_\odot$ (Panagia 1973; E. Green, private communication) and spectral type about O9. The stellar luminosity L_* inferred from the radio continuum is $\sim \frac{1}{3}$–$\frac{1}{2}$ the observed infrared luminosity. Several factors may help to explain this situation. First, the assumption of spherically symmetric emission may overestimate the actual luminosity if the energy source is near the front of the cloud (Natta *et al.* 1981). Second, the radio observations may underestimate L_* if more than one star is a significant ionization source or if there are optically thick components. Both these

TABLE 5

GAS AND DUST COOLING RATES

Shell No. (1)	T_K (K) (2)	Δv_i (pc^3) (3)	C_i(gas) ($L_\odot$) (4)	τ_i(FIR) (10^{-2}) (5)	C_i(dust) ($L_\odot$) (6)	τ_i'(FIR) (10^{-2}) (7)	C_i'(dust) ($L_\odot$) (8)
1	39	1.4	0.9	4.8	9 × 10^4	1.0	2 × 10^4
2	34	6.7	1.3	3.3	11 × 10^4	0.7	2 × 10^4
3	29	4.9	0.6	3.8	9 × 10^4	0.3	7 × 10^3
4	25	7.0	0.5	2.8	5 × 10^4	0.3	5 × 10^3
5	20	47	1.6	2.0	3 × 10^4	0.8	1 × 10^4
6	15	75	1.2	1.1	1 × 10^4	0.6	5 × 10^3
Sum, shells 1–6	...	...	6.2	...	3.8 × 10^5	...	7 × 10^4

situations may well exist in this case since the radio emission has a second, more compact component S88 B-2 which may be optically thick (Felli and Harten 1981). Third, dust may compete with the gas for absorption of Lyman continuum photons, resulting in an underestimate of L_* (cf. Jennings 1975). The exciting star of S88 A has a spectral type B0.5 V (Crampton, Georgelin, and Georgelin 1978), and thus could contribute only $2 \times 10^4\ L_\odot$. This star is not an important heat source, as is also apparent from the morphology of the CO maps.

VI. ENERGETICS: THE DETAILS

The availability of far-infrared data and CO $J = 2 \rightarrow 1$ data with comparable spatial resolution allows a more detailed examination of the energetics. The 50 and 100 μm data have been used to derive dust temperatures assuming a λ^{-1} emissivity law. The CO data taken with the OVRO antenna have been used to determine the kinetic temperature by assuming the $J = 2 \rightarrow 1$ transition is optically thick and thermalized. The results are presented in Figure 8 in the form of a grid of numbers. Rough contours of T_D and a few measurements of T_K are also shown in Figure 5 on the same scale as the other maps. Data exist for both T_K and T_D at three positions. At two of these positions T_D exceeds T_K by 5–12 K. At the third position, however, T_K exceeds T_D by 13 K. This is the position of highest T_K (52 K) in the map and also the position where the lowest T_D (39 K) is measured. This peculiar combination of circumstances suggests that observational error may play a role. The statistical errors on T_D and T_K are typically 2–3 K, but T_D can be biased to low values because the diffraction beam at 100 μm is significantly larger than that at 50 μm. Attempts to correct for this effect yield T_D at least 20% larger than those shown in Figure 8. Additional uncertainties in T_D of about 20% are caused by uncertainties in the emissivity law. Taken together, the uncertainties make it possible that $T_K < T_D$ at the position in question.

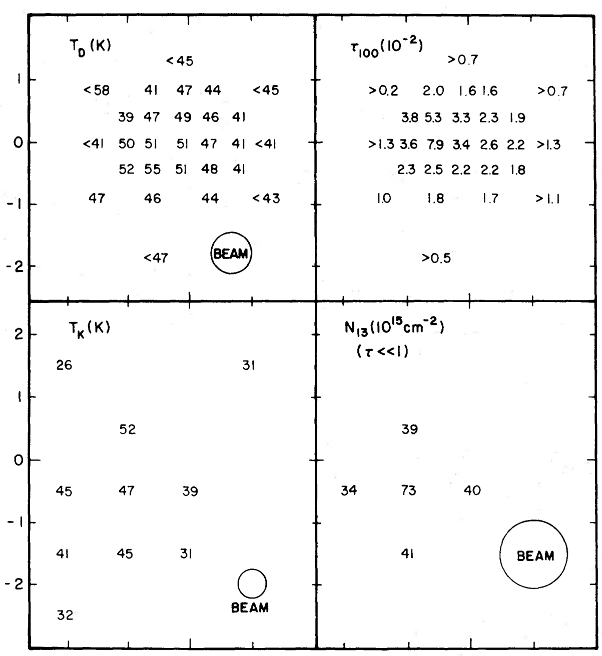

FIG. 8.—Maps of T_D, determined from the far-infrared data, and T_K, determined from the OVRO data. The dust optical depth at 100 μm is also shown.

Even if the necessary condition, $T_K < T_D$, is not violated, the S88 molecular cloud presents problems for the theory of Goldreich and Kwan (1974) because the density may be too low for the heating rate to balance the cooling rate. For $T_D - T_K = 10$ K and $T_K = 41$ K, the density required to balance the heating and cooling rates (Goldsmith and Langer 1978) is $n = 10^5$ cm^{-3}. At densities this high, the 2 mm line of H_2CO should be prominent in emission.

Pending further attempts to measure the density, one must suspect that the Goldreich-Kwan model in its simplest form may fail for the S88 molecular cloud. One possible solution is that the dust and gas are coupled through a mechanism besides collisions. In particular, Scoville and Kwan (1976) suggested that H_2O molecules absorb some of the far-infrared photons emitted by the dust and subsequent collisional deexcitation transfers this energy into kinetic energy of the gas molecules. More radical solutions are required if $T_K > T_D$. Then more direct ways to couple stellar energy into the gas may be necessary. In this connection, it is interesting to note that the position which appears to have $T_K > T_D$ has unusual CO profiles (Fig. 9). Both the $J = 1 \rightarrow 0$ (KP) and $J = 2 \rightarrow 1$ (OVRO) profiles are asymmetric, with a blue-shifted wing extending about 6 km s^{-1} from the line center. The $J = 2 \rightarrow 1$ profile has stronger emission in the blue-shifted wing, and the velocity of peak emission is also shifted to lower velocities relative to the $J = 1 \rightarrow 0$ peak. Some of these effects may be caused by differences in the beam size or pointing between the two measurements; consequently, we do not attempt a detailed analysis of optical depths, etc. Instead we simply note that a shock front moving toward the front of the cloud from the embedded H II region could produce such a wing. Heating by a shock front is thus a plausible explanation of the high T_K at this position.

The 50 and 100 μm data can be used to derive the dust optical depth at 100 μm, τ_{100}. As with the dust temperatures, a λ^{-1} emissivity law was assumed. The results are shown in Figure 8 along with T_D. The peak τ_{100} is 0.08, and the average over the region is 0.03. The relevant comparison is with τ_1(FIR) in column (5) of Table 5, which has a value of 0.048, in excellent agreement with the observations. ^{13}CO observations with higher spatial resolution would allow a more detailed comparison since τ_{100} varies by nearly an order of magnitude in the region of interest.

VII. SUMMARY

The S88 molecular cloud has been observed in a number of molecular lines and in the infrared. The CO emission encompasses S88 A and extends toward S88, but the only peak is centered near S88 B. The peak is

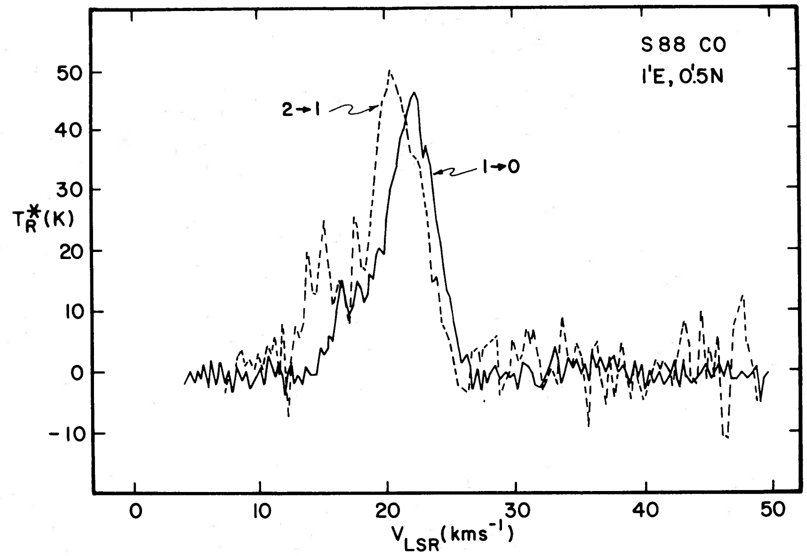

FIG. 9.—Spectra of the $J = 1\text{–}0$ (KP) and $J = 2 \rightarrow 1$ (OVRO) lines of CO in the direction 1′ E, 0′.5 N of the reference position. The Kitt Peak data have been scaled up by 30% (see § IIa) and divided by $\eta_{FSS} = 0.72$ to convert to T_R* for comparison to the OVRO data.

strong [T_A*(CO) > 30 K], and the emission falls off rapidly in all directions away from S88 B. The ^{13}CO map indicates that the column density peaks also near S88 B.

Extended infrared emission is found near the CO peak and has been mapped at 1.6, 2.2, 3.4, 50 and 100 μm. At the longer wavelengths the emission is centered on the compact H II region seen in the radio continuum. At shorter wavelengths, the emission peak shifts westward toward the visible Hα emission region S88 B. This behavior suggests a rapid increase in extinction beyond the eastern edge of the visible emission, which extinction may well hide the exciting star. At $\lambda > 1.6$ μm, the emission is more extended than the radio H II region and the integrated flux density exceeds that expected from the ionized gas. The energy distribution indicates the presence of dust at a wide range of temperatures.

The physical properties of the molecular cloud have been determined from the molecular line data. The size, measured to the T_A* = 10 K contour of CO emission, is 6.5 pc, and the mass is 5×10^3 $M_\odot$, both values applying at the assumed distance of 2 kpc. Average densities near the peak of $\sim 6 \times 10^3$ cm^{-3} are inferred. H_2CO emission at 2 mm is weak or absent, suggesting that the density does not reach values of 10^5 cm^{-3}. This result is somewhat surprising, since one component of the compact H II region appears to have $n_e \geq 1.9 \times 10^4$ cm^{-3} (Felli and Harten 1981).

The energetics of the molecular cloud have been explored using the standard techniques of this study. The gas cooling rate is 5–6 $L_\odot$. If the gas is heated by collisions with warm dust grains at $T_D > T_K$, the minimum predicted dust cooling rate is $0.7\text{–}3.8 \times 10^5$ $L_\odot$. The observed infrared luminosity is 1.8×10^5 $L_\odot$. This luminosity is 2–3 times larger than that inferred for the exciting star of the H II region.

While the predicted and observed dust cooling rates are in good agreement, the kinetic temperature may exceed the dust temperature at one position and even where $T_K < T_D$, rather high densities ($n \sim 10^5$ cm^{-3}) are required to balance gas heating and cooling rates. This requirement is in some conflict with the interpretation of the H_2CO results. Thus greater efficiency in coupling the dust energy into the gas kinetic energy may be required, or other heating mechanisms altogether may be necessary. The dust optical depth predicted from the ^{13}CO column density is in good agreement with the observations.

Many people have provided assistance with various aspects of this research. Bob Loren assisted with the MWO observations, Dan Nadeau and Steve Beckwith assisted with the Mount Wilson observations, and Ian Gatley and Mike Werner assisted with the observations on the Kuiper Airborne Observatory. We are also grateful to the staffs of the National Radio Astronomy Observatory, Kitt Peak National Observatory, the Mount Wilson Observatory, and the Kuiper Airborne Observatory. We thank Fred Gillett for assistance with the 2.1 m observations at Kitt Peak. We also thank Gerry Neugebauer for making available equipment and for logistical support at Mount Wilson. We thank Marcello Felli for making available data in advance of publication and for permission to reproduce Figure 5a.

The ^{12}CO(2–1) observations of S88 were obtained at OVRO by a team consisting of F. P. I., T. d. G., B. Fitton, H. Nieuwenhuyzen, S. Lidholm and A. I. Sargent. F. P. I. and T. d. G. would like to express their gratitude for the splendid cooperation by OVRO site personnel, in particular Ron Allen and Chuck Spencer. Thanks are also due to Russell Redman, Jill Knapp, and Tom Kuiper for invaluable assistance with pointing measurements and instrumental setup.

This work was supported in part by National Science Foundation grants AST 77-28475 and AST 79-2066 and by National Aeronautics and Space Administration grants NSG-7381 and NSG-2345 to The University of Texas at Austin, and by National Aeronautics and Space Administration grants NGR 03-002-390 to the University of Arizona and NGR 05-002-281 to the California Institute of Technology. A grant from the Research Corporation to The University of Texas at Austin also provided support. F. P. I. was supported by NSF grant AST 077-00247 to the Owens Valley Radio Observatory.

REFERENCES

Beckwith, S., Evans, N. J., II, Becklin, E. E., and Neugebauer, G. 1976, *Ap. J.*, **208**, 390.

Blair, G. N., Davis, J. H., and Dickinson, D. F. 1978, *Ap. J.*, **226**, 435.

Blair, G. N., Evans, N. J., II, Vanden Bout, P. A., and Peters, W. L., III. 1978, *Ap. J.*, **219**, 896 (Paper II).

Blair, G. N., Peters, W. L., III, and Vanden Bout, P. A. 1975, *Ap. J.* (*Letters*), **200**, L161.

Crampton, D., Georgelin, Y. M., and Georgelin, Y. P. 1978, *Astr. Ap.*, **66**, 1.

Davis, J. H., and Vanden Bout, P. A. 1973, *Ap. Letters*, **15**, 43.

Deharveng, L., and Maucherat, M. 1978, *Astr. Ap.*, **70**, 19.

Dickman, R. 1978, *Ap. J. Suppl.*, **37**, 407.

Evans, N. J., II, Beichman, C., Gatley, I., Harvey, P., Nadeau, D., and Sellgren, K. 1981, *Ap. J.*, in press.

Evans, N. J., II, and Blair, G. N. 1981, *Ap. J.*, in press (Paper III).

Evans, N. J., II, Blair, G. N., and Beckwith, S. 1977, *Ap. J.*, **217**, 448. (Paper I); Erratum 1978, *Ap. J.*, **222**, 382.

Felli, M., and Harten, R. H. 1981, *Astr. Ap.*, in press.

Ferland, G. J. 1980, *Pub. A.S.P.*, **92**, 596.

Georgelin, Y. M. 1975, thesis, University of Marseille.

Goldreich, P., and Kwan, J. 1974, *Ap. J.*, **189**, 441.

Goldsmith, P. F., and Langer, W. D. 1978, *Ap. J.*, **222**, 881.

Harvey, P. M. 1979, *Pub. A.S.P.*, **91**, 143.

Jennings, R. E. 1975 in H II *Regions and Related Topics*, ed. T. L. Wilson and D. Downes (Berlin: Springer-Verlag), p. 137.

Kutner, M. L., and Ulich, B. L. 1981, *Ap. J.*, submitted.

Leighton, R. B. 1978, Final Technical Report for NSF project AST 73-04908.

Lidholm, S., and de Graauw, T. 1979, in *Fourth International Conference on Infrared and Millimeter Waves and Their Applications*, ed. S. Perkowitz (IEEE Cat. No. 79 CM 1384. 7 MTT), Appendix p. 38.

Lortet-Zuckerman, M. C. 1974, *Astr. Ap.*, **30**, 67.

Matsakis, D. N., Evans, N. J., II, Sato, T., and Zuckerman, B. 1976, *A.J.*, **81**, 172.

Natta, A., Palla, F., Panagia, N., and Preite-Martinez, A. 1981, *Astr. Ap.*, in press.

Panagia, N. 1973, *A.J.*, **78**, 929.

Pipher, J. L., Sharpless, S., Savedoff, M. P., Krassner, J., Varlese, S., Soifer, B. T., and Zeilik, M. 1977, *Astr. Ap.*, **59**, 215.

Price, S. D., and Walker, R. G. 1976, AFGL Report AFGL-TR-76-0208.

Schwartz, P. R., Wilson, W. J., and Epstein, E. E. 1973, *Ap. J.*, **186**, 529.

Scoville, N. Z., and Kwan, J. 1976, *Ap. J.*, **206**, 718.

Sharpless, S. 1959, *Ap. J. Suppl.*, **6**, 257.

Silverglate, P. R., and Terzian, Y. 1978, *Ap. J.*, **224**, 437.

Snell, R. 1981, *Ap. J. Suppl.*, **45**, 121.

Turner, B. E. 1970, *Ap. Letters*, **6**, 99.

Ulich, B. L., and Haas, R. W. 1976, *Ap. J. Suppl.*, **30**, 247.

Viner, M. R., Clarke, J. N., and Hughes, V. A. 1976, *A.J.*, **81**, 512.

Wendker, H. J. 1971, *Astr. Ap.*, **13**, 65.

Whitcomb, S. E., Hildebrand, R. H., and Keene, J. 1980, *Pub. A.S.P.*, in press.

Wilson, T. L., Snell, R., and Vanden Bout, P. A. 1981, in preparation.

Wright, E. L. 1976, *Ap. J.*, **210**, 250.

Zeilik, M. 1977, *Ap. J.*, **213**, 58.

Note added in proof.—A drift in the second local oscillator used for the $J = 2 \rightarrow 1$ CO data obtained at OVRO has been discovered. The $J = 2 \rightarrow 1$ spectrum in Figure 9 should be shifted by 1.3 km s^{-1} to higher velocities. This shift brings the spectrum into better agreement with the $J = 1 \rightarrow 0$ spectrum. None of the conclusions in the paper are affected.

Recently Armandroff and Herbst (submitted to *A.J.*) have estimated the distance to the S88 molecular cloud by a star counting method to be 2.81 ± 0.17 kpc. If this distance is assumed to be correct, the size of the cloud becomes 9 pc, the mass becomes $10^4\ M_\odot$, and the highest $\langle n \rangle$ is 4×10^3 cm^{-3}. The total gas cooling rate would be 17 $L_\odot$, while the predicted dust cooling rate becomes $1.4–7.5 \times 10^5\ L_\odot$, and the observed dust cooling rate would be $3.6 \times 10^5\ L_\odot$. The flux of Lyman continuum photons inferred from the radio would be 4.1×10^{48} s^{-1}, corresponding to a stellar luminosity of $L_* = 10^5\ L_\odot$ and spectral type of O7 to O8. None of the basic arguments in the paper would be altered.

G. N. Blair: ElectroMagnetic Applications, Inc., P.O. Box 26263, Denver, CO 80226

T. de Graauw and F. Israel: Space Science Division, European Space Agency, ESTEC, Postbus 299, 2200 AB Noordwijk ZH, The Netherlands

N. J. Evans, II, P. Harvey, W. L. Peters, III, M. Scholtes, and P. Vanden Bout: Department of Astronomy, The University of Texas at Austin, Austin, TX 78712